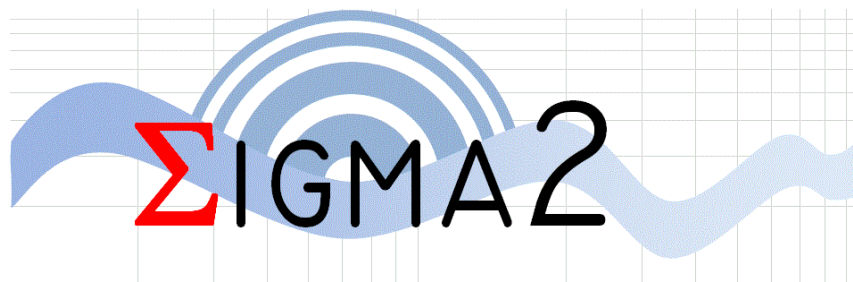
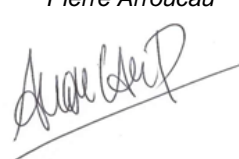
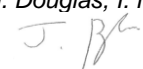
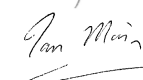
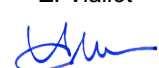


	<p>Research and Development Program on Seismic Ground Motion</p>	<p>Ref : SIGMA2-2018-D2-014</p>
		<p>Version : 2</p>

A preliminary three-dimensional seismological model of the crust and uppermost mantle for Metropolitan France

Work Package #2 “Earthquake parameters”



AUTHORS		REVIEW		APPROVAL	
Name	Date	Name	Date	Name	Date
<i>Pierre Arroucau</i> 	2020/03/03	<i>J. Douglas, I. Main</i>  	2020/03/05	<i>E. Viallet</i>  Public access ✓ SIGMA-2 restricted	2020/12/21

DISSEMINATION: This document must not be distributed to any person, institution or company other than members of SIGMA-2 steering and scientific committees, except under written formal permission of SIGMA-2 steering committee.

Document history

DATE	VERSION	COMMENTS
2018/08/15	1.0	
2020/03/03	2.0	

Executive summary

We present a new three-dimensional (3D) seismological P- and S-wave speed model of the crust and uppermost mantle for Metropolitan France (i.e. the part of France located in Europe) and neighboring countries, primarily aimed at earthquake location. The model extends from 8°W to 13°E in longitude and 40°N to 52°N in latitude, and from the earth's surface down to 100 km depth. It is parameterized on a regular, 10 km x 10 km x 0.5 km grid and includes two explicit interfaces: the topography/bathymetry, which we set to that of ETOPO1, and the crust-mantle boundary that we model from previously published controlled-source seismics and receiver function studies by means of a probabilistic surface reconstruction technique. The modeled Moho depths range from 14 to 54 km, which is consistent with the current tectonic setting of France that encompasses regions of thinned continental crust and thickened orogenic areas. Our reference model for P- and S-wave speeds in the crust is EPcrust (Molinari and Morelli, 2011), which we combine with recently published tomographic models by weighted average. When only P- or S-wave speed is available, the other quantity is calculated using a V_p/V_s value of 1.70, and the resulting model is assigned a lower weight than the original one. A similar weighted average model is used for the mantle, however the V_p/V_s ratio is inferred from ak135 model. Information from P_n and S_n tomography is also incorporated, with a weight decreasing from 0.5 at Moho depth to 0.0 at 60 km. The final model is accompanied with a 3D weighted standard deviation grid for both V_p and V_s , which provides a quantitative estimate of wave speed uncertainties. The resulting model shows significant deviations from a one-dimensional (1D) model, with lateral variations ranging from ~1-2 % in the mantle up to ~20% in the upper crust. This model can readily be used to produce homogeneous locations of earthquakes in Metropolitan France and neighbouring areas, although its actual potential for hypocentral solution quality improvement still needs to be assessed. This model can also be used as a starting model for local earthquake tomography or to correct for crustal effects in teleseismic tomography.

Introduction

Metropolitan France, i.e. the part of France located in Europe, is recognized as a region of relatively moderate seismicity, both in terms of magnitudes and number of events, as testified by historical and instrumental observations (Cara et al., 2015; Manchuel et al., 2018). Although seismic hazard is also low (e.g. Giardini et al., 2014), it is nonetheless a significant subject of concern due to the presence of several critical facilities -more particularly nuclear power plants- over the territory. In such a region, where known active faults are rare, seismic hazard assessment essentially relies on earthquake catalogue analysis and requires accurate seismic event locations and magnitude estimates. Since the early 1960s, the development of seismological networks aimed at monitoring earthquake activity in the area has progressively led to an increase in detection capability and hypocentral parameter estimation quality.

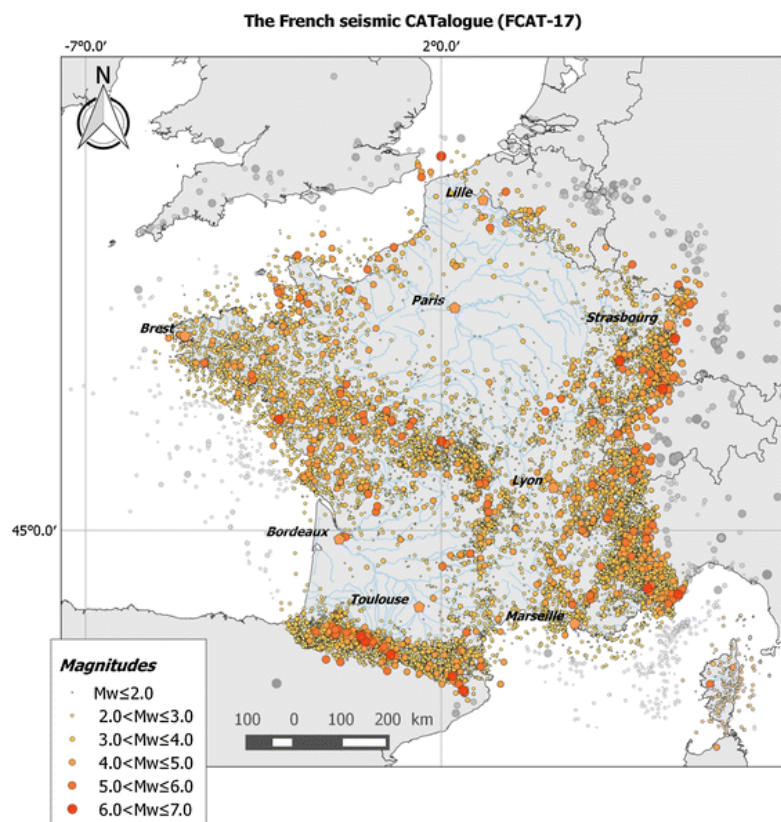


Figure 1. Combined historical (AD463-1965) and instrumental (1965-2009) seismicity map of Metropolitan France (from Manchuel et al., 2018).

Earthquake locations reported in catalogues are traditionally obtained by means of P- and S-wave travel time inversion considering a one-dimensional (1D), layered medium (e.g. Lienert et al., 1986), thus assuming that lateral wave speed variations can be neglected. Yet, due to its current geodynamic setting and to a complex geological history, the structure of Metropolitan France is barely 1D and is instead characterized by lateral variations of lithology, topography and crustal thickness that, if taken into account, could lead to improved hypocentral solutions.

In this report, we present an attempt to produce a unified, preliminary 3D P- and S-wave speed model of the crust and upper mantle for Metropolitan France. The resulting model integrates information from recently published active and passive seismic imaging studies. It is primarily designed for earthquake hypocentral parameter estimation but could also be used as *a priori* starting model in future local earthquake tomographic investigations.

1. Objectives and model characteristics

Our study area spans from 8°W to 13°E in longitude and 40°N to 52°N in latitude. It thus extends beyond the borders of Metropolitan France, which should facilitate the use of trans-border signals to locate any seismic source, regardless of receiver location. Since the distances involved could possibly imply rays turning in the mantle at depths as low as 80 km depth, the model extends from the surface down to 100 km below sea level. Grid node spacing is 0.130° in longitude and 0.090° in latitude at all depths, approximately corresponding to 10 km at sea level, in both directions. Grid node spacing is 0.5 km in the vertical direction. Note that, in this work, all depths are expressed with respect to sea level

The region presents significant topography and bathymetry variations that also need to be accounted for: earthquakes occur both onshore and offshore so a given event can for instance be recorded at a station located in the Alps and at another one located on the Ligurian Sea floor, with several kilometers of elevation difference between them. As a result, using a 1D model could potentially alter the quality of hypocentral solutions, both in terms of accuracy and precision. Furthermore, seismic phases present in earthquake catalogues not only consist of first P- and S-wave arrivals, but sometimes also contain secondary arrivals, so both Pg (direct, crustal) and Pn (refracted at the crust-mantle boundary) phases may have been picked for a given event at the same station. Although classical 3D travel time calculation codes are only able to compute first arrivals, some allow the calculation of additional phases (e.g. Rawlinson et al., 2006). Wagner et al. (2013) have for instance shown that including Pg, Pn and PmP (crustal phases reflected off the crust-mantle boundary) could improve earthquake hypocentral locations. Our model therefore includes two explicit interfaces: (1) the topography/bathymetry and (2) the crust-mantle boundary (or Mohorovičić discontinuity, or Moho), and the crust and mantle are modelled separately.

2. Model inputs

We exploit various models from previous passive and active seismic imaging studies. Topography and bathymetry are defined from ETOPO1 (Amante and Eakins, 2009), while Moho depth variations are essentially constrained using (1) controlled-source seismic (CSS) experiment results collected by several authors (Chamot-Rooke et al., 1997 ; Chevrot et al., 2015 ; Diaz and Gallart, 2009 ; Licciardi, 2016 ; Lombardi et al., 2008 ; Sichien et al., 2012) and (2) results from receiver function analysis (Chevrot et al., 2015 ; Geissler et al., 2008 ; Knapmeyer-Endrun et al., 2014 ; Licciardi, 2016 ; Mancilla et al., 2015 ; Mele et al., 2013 ; Spada et al., 2013 ; Stipčević et al., 2011), but also (3) surface wave tomography (Yudistira, 2015) and (4) local earthquake data analysis (Sichien et al., 2012). All these models are listed in Table 1, along with their respective characteristics.

Crustal seismic structure is obtained by combining information from EPcrust reference model (Molinari and Morelli, 2011) with that from ambient noise and teleseismic surface wave tomography models (Gaudot, 2016 ; Kästle et al., 2018 ; Lu et al., 2018 ; Macquet et al., 2018 ; Palomeras et al., 2017 ; Pasyanos et al., 2014), from the CSS-derived model of Kelly et al. (2007) and from a local earthquake tomography study (Diehl et al., 2009). Note that the tomographic models of Theunissen et al. (2018) and Potin (2016), respectively for the Pyrenees and the Alps, could not be obtained from their authors because they have not been published separately from other work yet. Theunissen however provided us with their *a priori* model, based on geological and geophysical studies, which we used in this work.

Our mantle model also incorporates results from Pn and Sn tomography (Diaz et al., 2013), from teleseismic P-wave traveltimes residual tomography (Amaru, 2007 ; Bezada et al., 2014 ; Chevrot et al., 2014 ; Monna et al., 2013) as well as ambient noise and teleseismic surface wave tomography (Kästle et al., 2018 ; Lu et al., 2018 ; Palomeras et al., 2017 ; Pasyanos et al., 2014 ; Schivardi and Morelli, 2011). All the tomographic studies that were used to model either the crust or the mantle are presented

in Table 2. They are also shown in Fig. 2 with their respective confidence regions, either provided by their authors or deduced from sensitivity tests presented in the corresponding publications. Any model that could be obtained was used, without exclusion criteria.

Reference	Type	n _{obs}	uncertainties (Y/N)	Multiplicative constant
Chamot-Rooke et al. (1997)	CSS	31	N	1.33
Chevrot et al. (2015)	CSS	19	N	0.85
Chevrot et al. (2015)	RF	265	N	2.64
Diaz and Gallart (2009)	CSS	243	N	2.16
Geissler et al. (2008)	RF	10	N	2.16
Knapmeyer-Endrun et al. (2014)	RFP	297	Y	2.40
Knapmeyer-Endrun et al. (2014)	RFS	60	Y	1.57
Licciardi (2016)	BRF	25	N	2.16
Licciardi (2016)	SRF	11	N	2.04
Licciardi (2016)	REFL	99	N	0.98
Licciardi (2016)	REFR	43	N	1.09
Lombardi et al. (2008)	CSS	57	Y	1.45
Mancilla et al. (2015) - a	RF	85	N	1.45
Mancilla et al. (2015) - b	RF	68	N	2.88
Mele et al. (2013)	RF	15	N	4.42
Sichien et al. (2012)	EQ, CSS	22	Y	1.33
Spada et al. (2013) - 0	RF	10	N	3.35
Spada et al. (2013) - 1	RF	47	N	1.33
Spada et al. (2013) - 2	RF	41	N	4.41
Spada et al. (2013) - 4	RF	13	N	2.4
Stipčević et al. (2011)	RF	2	N	0.5
Yudistira (2015)	SWT	54	Y	0.74

Table 1. Passive and active source models used to constrain Moho depth lateral variations. References are indicated with quality factor, when relevant, as well as model types, (CSS: controlled source seismics ; RF: receiver functions ; RFP: P-receiver functions ; RFS: S-receiver functions ; BRF : broadband receiver functions ; SRF: short period receiver functions ; REFL : reflection seismics ; REFR: refraction seismics ; EQ: earthquake data interpretation ; SWT: surface wave tomography), the number of points available (nobs), whether or not uncertainties have been estimated, and the value of the data error multiplicative constant derived from the surface reconstruction algorithm (see text for details).

CRUST			
Reference	Model type	Depth range (km)	Weight (P - S)
Diehl et al. (2009)	LET	- / 80	1.0 / 0.25
Gaudot (2016)	ANT	0 / 60	0.25 / 0.75
Kästle et al. (2018)	ANT-TSWT	0 / 200	0.5 / 1.0
Kelly et al. (2007)	CSS compilation	0 / 60	0.5 / 0.125
Lu et al. (2018)	ANT	0 / 80	0.125 / 0.25
Macquet et al. (2014)	ANT	0 / 46	0.25 / 0.75
Molinari and Morelli (2011)	Compilation of previous models	- / 50	0.1 / 0.1
Palomeras et al. (2017)	ANT-TSWT	0 / 250	0.25 / 0.75
Pasyanos et al. (2014)	TSWT	- / 400	0.05 / 0.05
MANTLE			
Reference	Data type	Depth range (km)	Weight (P-S)
Bezada et al. (2014)	TT	10 / 690	1.0 / 0.25
Chevrot et al. (2014)	TT	12.5 / 600	1.0 / 0.25
Kästle et al. (2018)	ANT-TSWT	0 / 200	0.25 / 1.0
Lu et al. (2018)	ANT	0 / 80	0.25 / 1.0
Monna et al. (2013)	TT	0 / 600	1.0 / 0.25
Palomeras et al. (2017)	ANT-TSWT	0 / 250	0.25 / 1.0
Pasyanos et al. (2014)	TSWT	- / 400	0.1 / 0.1
Schivardi and Morelli (2011)	TSWT	60 / 490	0.25 / 1.0
Amaru (2007)	TT	5/2815	1.0 / 0.25

Table 2. List of models used to build our crust and uppermost mantle seismological model of Metropolitan France. Model type refers to the type of data and tomographic method used (TT: teleseismic P-wave travelttime residual tomography ; ANT: ambient noise tomography ; TSWT: teleseismic surface wave tomography). The depth range of the original model is indicated. P- and S- weights used in the model integration procedure are also reported, with bold font showing the original wave type of the model, while normal font is used if the model was calculated using an empirical Vp/Vs ratio value (1.70 for the crust, from ak135 in the mantle).

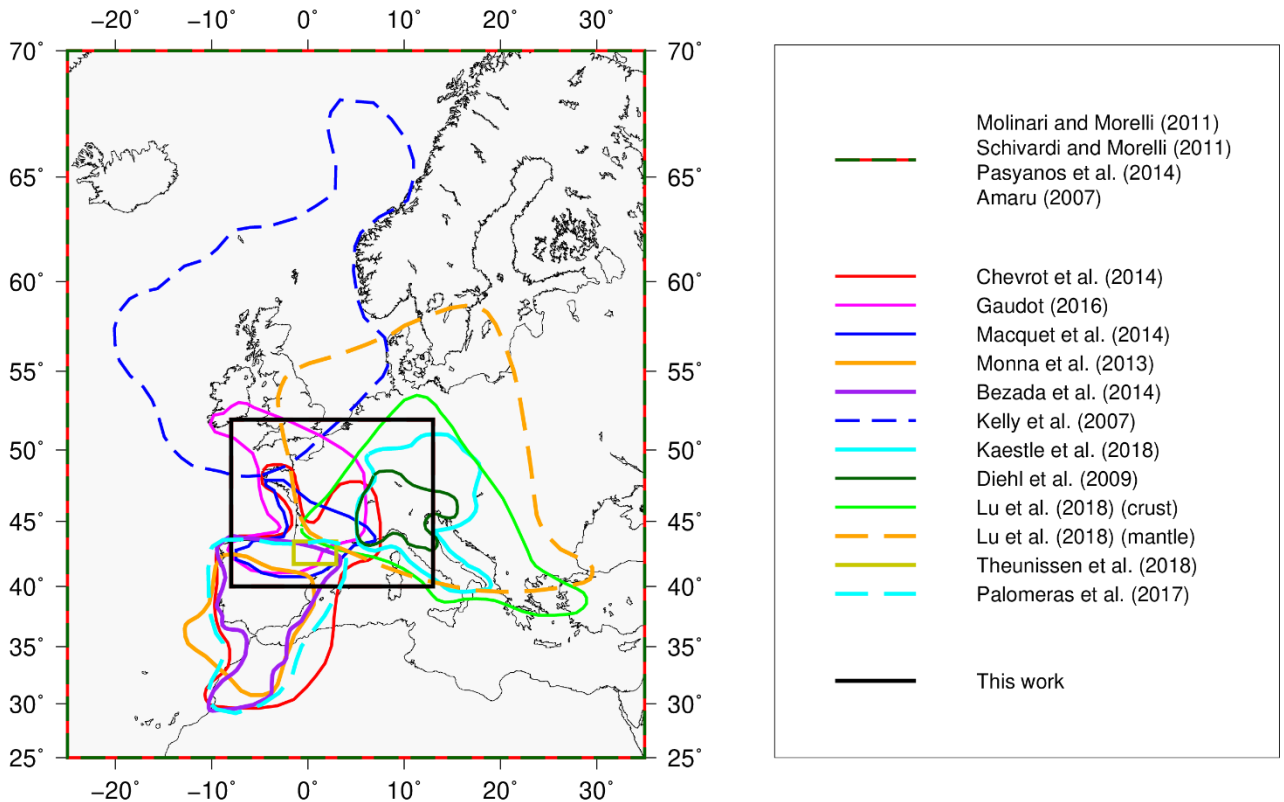


Figure 2. Spatial extent and confidence region of the models used in this work. See text for details.

3. Model integration

We use EPcrust (Molinari and Morelli, 2011) as our reference, which we modify to integrate additional information from other models. EPcrust is a crustal model of the European Plate defined on a $0.5^\circ \times 0.5^\circ$ grid. It is designed from a compilation of previous studies and consists of three layers, namely sediments, upper crust and lower crust, for which laterally varying thickness, P- and S-wave speed and density, are provided. It also includes a topographic grid from which thicknesses can be converted to depths. Fig. 3 and 4 show horizontal slices for both V_p and V_s , respectively, at depths ranging from 0 to 40 km. Note that since EPcrust is a crustal model, it does not provide wave speeds for the mantle. We first resample EPcrust on a $10 \text{ km} \times 10 \text{ km} \times 0.5 \text{ km}$ grid using a bicubic interpolation scheme. Then, we substitute its topography and bathymetry by that of ETOPO1 (Amante and Eakins, 2009), a global 1 arc-minute topographic model, which we also resample after application of a lowpass filter to avoid aliasing (Fig. 5). Moho depth grid is also modified to account for controlled source compilations and recent receiver function studies (Table 1). To that end we use a modified version of the probabilistic surface reconstruction algorithm of Bodin et al. (2012). The reconstruction problem is solved in a Bayesian framework by means of the reversible jump Markov chain Monte Carlo (MCMC) algorithm (Green, 1995, 2003).

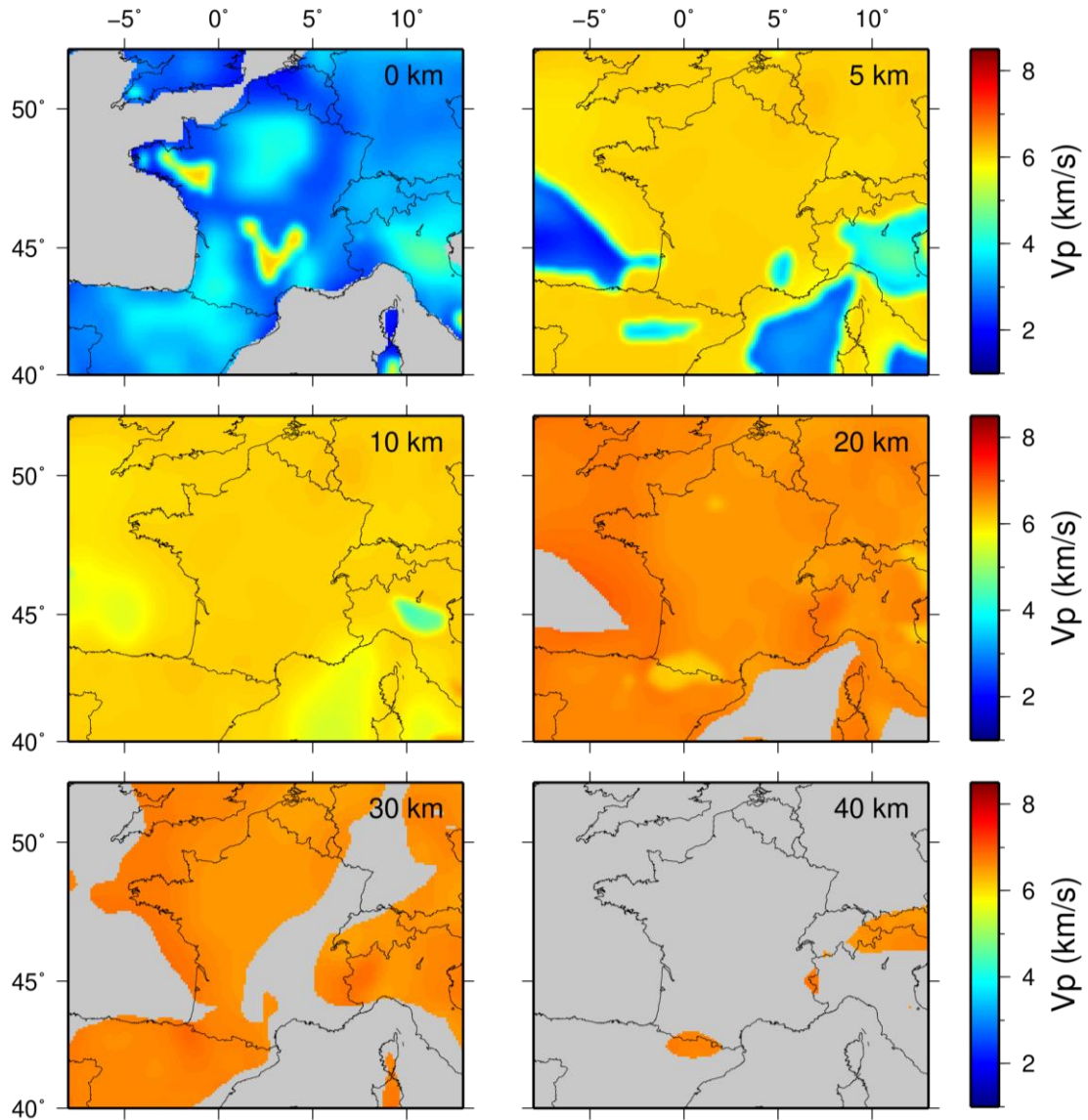


Figure 3. P-wave speed horizontal slices through EPcrust reference model. Grey areas correspond to the mantle, for which EPcrust does not provide any wave speed values. Note that the 10 km x 10 km grid has been resampled to 1 km x 1 km for display purpose.

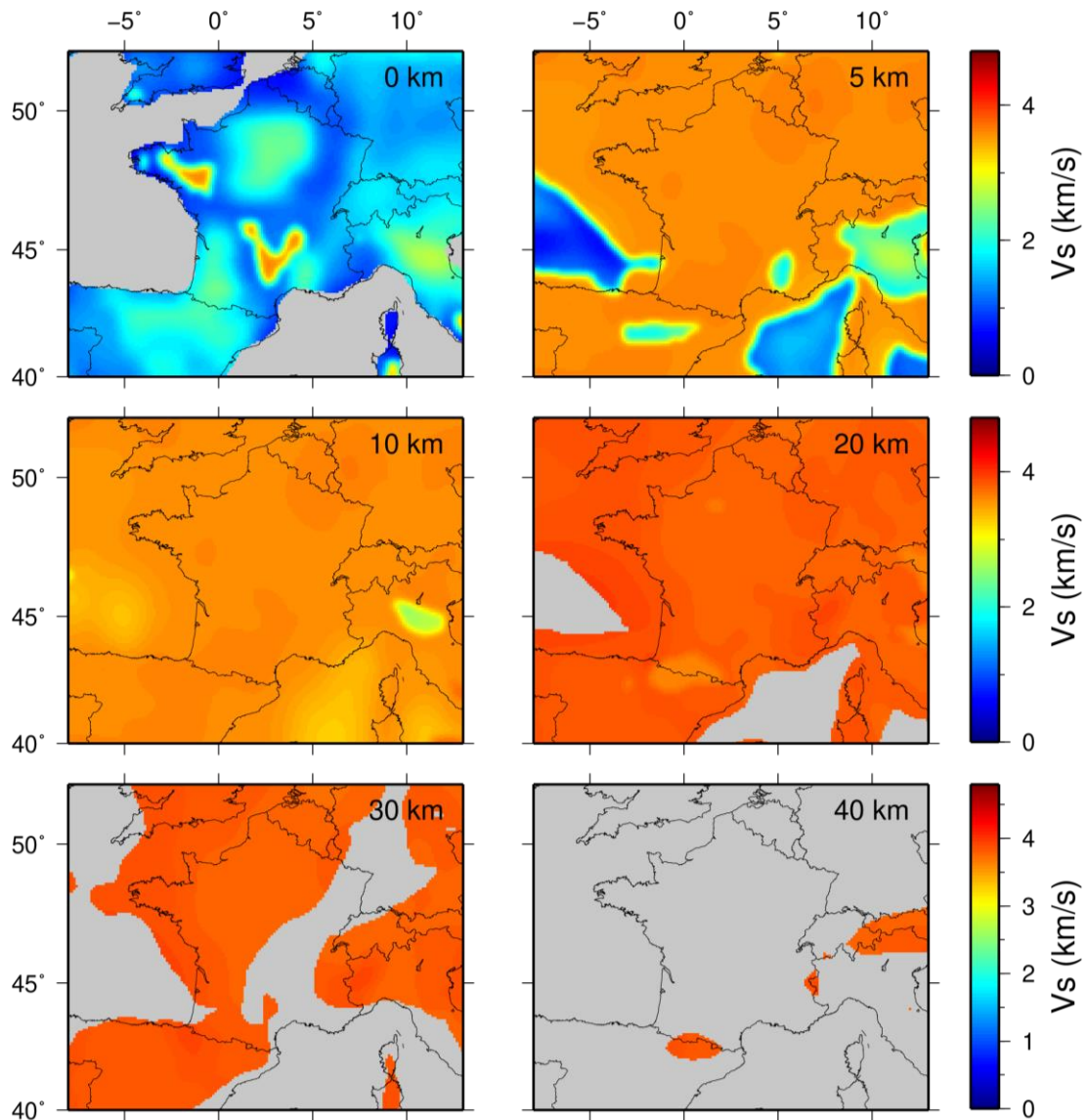


Figure 4. S-wave speed horizontal slices through EPcrust reference model. Grey areas correspond to the mantle, for which EPcrust does not provide any wave speed values. Note that the 10 km x 10 km grid has been resampled to 1 km x 1 km for display purpose.

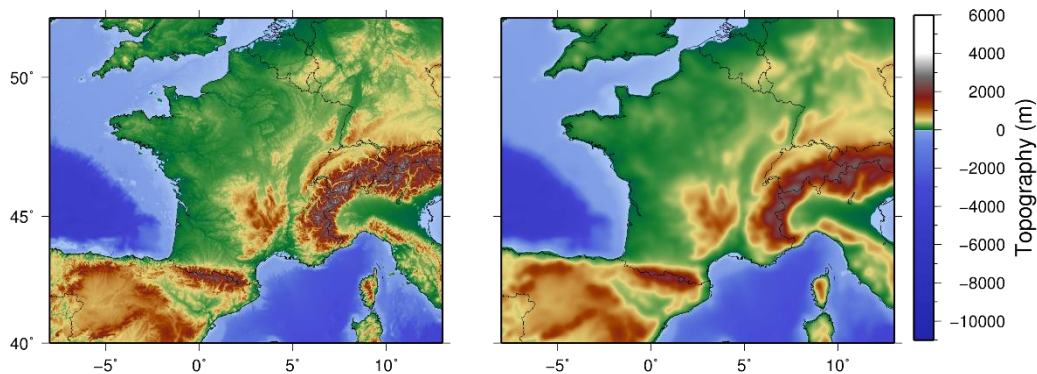


Figure 5. Left: ETOPO1 topographic and bathymetric 1 arc-minute model (Amante and Eakins, 2009). Right: same model resampled on a 10 km x 10 km grid (here subsequently resampled at 1 km for display purpose).

The surface to infer is modeled by means of a set of Voronoi cells whose number is not fixed but instead is allowed to vary in the course of the procedure, based on the information present in the data (see Fig. 6 for an example). The result is an ensemble of solutions from which statistical estimates (such as the mean, median, mode, standard deviation, etc.) can be calculated. An additional feature of the algorithm is that the noise affecting the data can also be considered as an unknown and determined by the procedure. Here, when data errors are indicated by the authors (Table 1), we simply determine the value of a multiplicative constant that needs to be applied to the noise for that specific dataset. When data error estimates are missing, we set the error value to 1.0 for the entire dataset and proceed in a similar way. More details about the methodology can be found in Bodin et al. (2012).

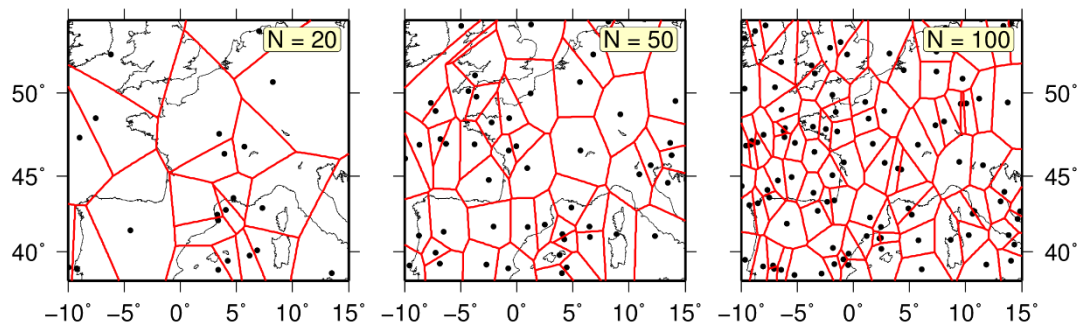


Figure 6. Examples of random Voronoi cell tessellation configurations for three different cell numbers indicated in the upper right corner of each subfigure.

We first build our reference surface by combining EPcrust Moho with that from Spada et al. (2013), which is used here as Moho depth reference for the Alpine area (Fig. 7). The reason for this is that Spada's model incorporates CSS data that we could not obtain and that constrain fine variations of Moho depth in the Alps. Then, we express input Moho depth values (Table 1) as anomalies with respect to the reference surface (Fig. 8) by simple subtraction, after conversion from crustal thickness to Moho depth whenever needed. After reconstruction, the resulting depth anomaly surface, calculated as the mean of the posterior distribution, is added back to the reference to produce our final Moho depth model. Results are summarized in Fig. 8. In addition to the mean depth, we also compute a standard deviation map, which can be interpreted as a representation of Moho depth uncertainty. (Fig. 9).

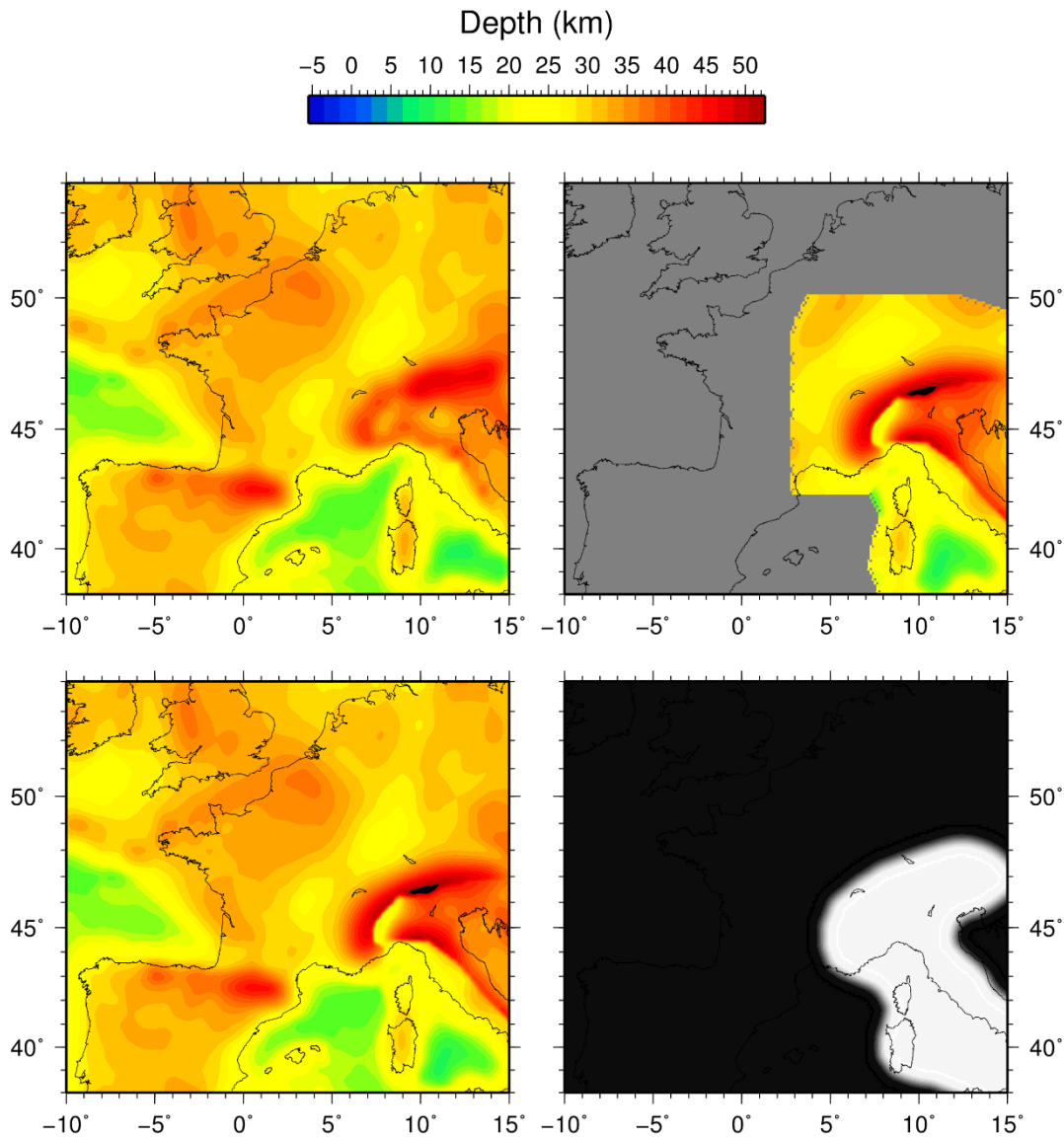


Figure 7. Construction of the Moho depth reference surface. It consists in the combination of EPcrust Moho (Molinari and Morelli, 2011) shown on the upper left panel with that from Spada et al. (2013) for the Alpine region (upper right). The lower left panel shows the weighting function that was applied to Spada's model, with a weight ranging from 0.0 (black) to white (1.0). The resulting model is shown on the lower left.

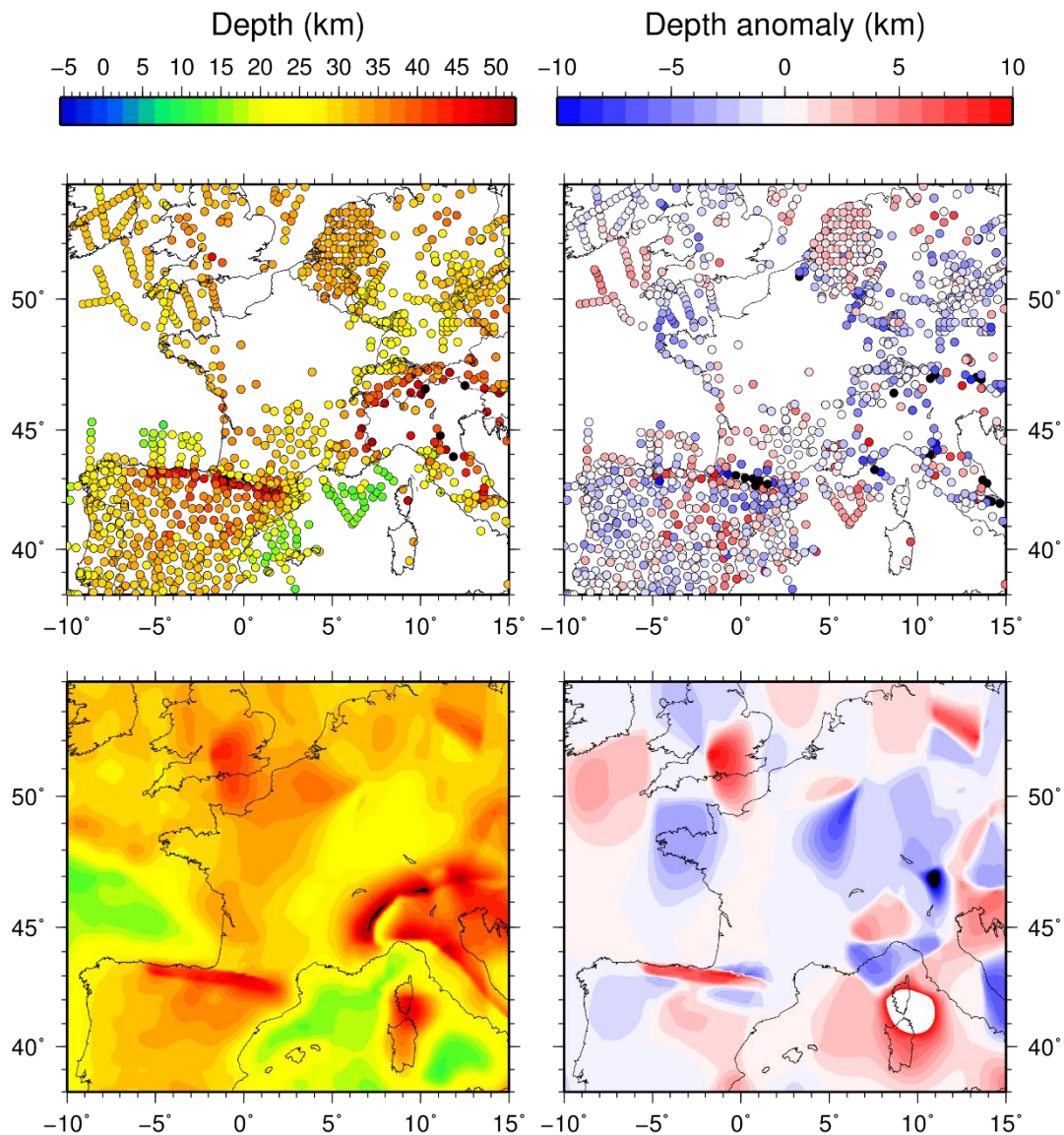


Figure 8. Upper left: Moho depth measurements from receiver function and controlled source seismic studies (see Table 1 for references). Upper right: Moho depth anomaly, calculated as the difference between depth measurements and the combined reference Moho depth of EPcrust (Molinari and Morelli, 2011) and Spada et al. (2013) for the Alps. Lower right: Moho depth anomaly surface, reconstructed by means of the method of Bodin et al. (2012). Lower left: Moho depth map obtained by adding the anomaly surface to the reference one.

Once topography and crust-mantle boundary have been modeled, we modify EPcrust as follows: sediment thickness is left unchanged; upper and lower crust, on the other hand, are transformed using the new-to-old crustal thickness ratio (without sediments), so their relative thicknesses are preserved. Note that a similar transformation is applied to the crustal part of Litho1.0 (Pasyanos et al., 2014), which is also defined by layers and interfaces, including explicit topography and crust-mantle boundary. We combine the modified EPcrust model with the 3D wave speed grids from the tomographic studies listed in Table 2 by calculating their weighted average, yet excluding values greater than 7.5 km/s for P-waves and 4.2 km/s for S-waves in order to avoid mantle wave speeds. Prior to the averaging process, all models were first resampled in the horizontal directions on a 10 km x 10 km grid using bicubic interpolation, then linearly interpolated in depth so as to obtain a horizontal slice every 0.5 km.. We use

the confidence regions shown in Fig. 2 to define the regions of full weight, which are subsequently smoothed out by convolution with a Gaussian kernel, with a 50 km standard deviation. Full weight values are given in Table 2. A specific, depth-dependent weighting scheme is applied to EPcrust: its weight linearly decreases from full weight at Moho depth to one third of that value at 0 km depth, to mitigate the effect of relatively low resolution of ambient noise and local earthquake tomography in the deep crust.

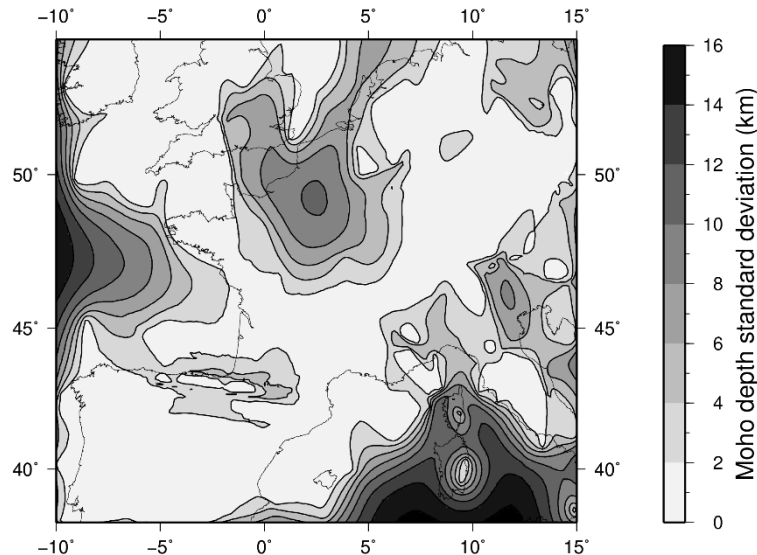


Figure 9. Map of the Moho depth a posteriori standard deviation calculated from the ensemble solution and expressed in percent of the mean depth value shown in Fig. X.

Although the advent of ambient noise cross-correlation technique and tomography (e.g. Shapiro et al., 2005) has with no doubt resulted in a significant step forward for crustal imaging, providing unprecedented high resolution wave speed models in regions of low seismicity, ambient noise correlation is often carried out on the vertical component only so Love waves are missed and the 3D models inferred from those measurements are shear wave speed models only. Conversely, first P-wave arrivals being easier to pick on seismograms than S phases, local earthquake tomographic inversions are sometimes only performed for P-waves, so their S-wave counterpart is often missing. In order to maintain a certain level of mutual consistency between our P- and S-wave speed models, whenever only P- or S-wave speed is available the other is calculated using a V_p/V_s ratio value of 1.70, and a lower weight is assigned to the quantity obtained by calculation.

The mantle component of our model is also constructed as a weighted average of models from the body and surface wave tomography studies listed in Table 2, resampled on a 10 km x 10 km x 0.5 km grid. V_p/V_s ratio is taken from ak135 model (Kennett et al., 1995) at any depth to calculate P- and S-wave speeds from one another when needed. Like for the crust, P- and S-wave speed values respectively lower than 7.5 km/s and 4.2 km/s are excluded from the calculation (in other words are assigned a weight of 0.0). Weighting is also applied to each model in a similar fashion to that used for the crust, yet with a smoothing Gaussian kernel standard deviation of 100 km instead of 50 km. An additional, depth dependent weighting factor is used to avoid artificial discontinuities due to models that would not extend down to the bottom of our grid. It is for instance the case of the model by Lu et al. (2018), only defined down to 80 km depth (see Table 2). That weight, w_{zmax} , writes: $w_{zmax} = \exp - \left\{ \frac{5 z^2}{z_{max}^2} \right\}$, where z is the depth in km and z_{max} the maximum depth at which that model is defined, also in km. It is therefore equal to 1.0 at 0 km depth, and decreases to ~ 0.007 at z_{max} . Finally, we also incorporate the Pn and Sn models of Diaz et al. (2013) with a specific, depth-dependent weight w_{Diaz} , whose expression is

similar to that of w_{zmax} , so that: $w_{Diaz} = 0.5 \exp - \left\{ \frac{5(z-zmoho)^2}{(60-zmoho)^2} \right\}$, where z is the depth and $zmoho$ is moho depth, both expressed in km. Thus, similarly, this weight is equal to 0.5 at Moho depth, and decreases to a value of ~ 0.003 at 60 km.

In order to quantify the uncertainty associated with this model, the weighted standard deviation σ_V is computed for both V_p and V_s at each node of the 3D grid as :

$$\sigma_V = \sqrt{\frac{M \sum_{i=1}^N \omega_i (V_i - \bar{V})^2}{M - 1 \sum_{i=1}^N \omega_i}}$$

where \bar{V} is the weighted mean, M the number of non-zero weights, N the number of input values used to compute the mean at that node, V_i the i^{th} input value and ω_i its associated weight. The calculated value essentially represents the input wave speed variability at each node. It accounts for the spatial coverage and relative weight of each model. Note that it is probably different from what would be obtained from uncertainty propagation. Unfortunately, seismic tomography studies found in the literature are rarely -if at all- accompanied with uncertainty estimates, thus precluding that type of calculation.

4. Results and discussion

We present our model through a series of horizontal slices showing wave speed maps and their associated relative uncertainties at different depths (Fig. 10 and 11 for P- and Fig. 12 and 13 for S-waves respectively), as well as a set of North-South (Fig. 14 and 15 for P- and S-waves, respectively) and East-West cross-sections (Fig. 16 and 17 for P- and S-waves, respectively).

Although it is not the purpose of this model to be used for structural interpretation, it is worth noting that the main structural and morphological regions show a specific signature. For instance the Armorican and Central Massifs can be identified by higher wave speeds than the surrounding Paris and Aquitanian Basins at 0 km depth. Similarly, the internal zones of the Alps are also characterized by relatively high wave speeds that contrast with the low velocities of the Po Plain, the Molasse Basin or the southern part of the Rhône Valley. At 5 km depth, the largest contrasts occur in continental margin settings, such as the Liguro-Provençal Basin or the Bay of Biscay. Moho depth variations are responsible for the strongest horizontal wave speed gradients, as visible for instance at 20 km depth. The depth slices and cross-sections shown in Figs. 6 to 11 illustrate the lateral wave speed variations that occur throughout the entire domain of Metropolitan France, thus providing evidence that it is certainly not 1D.

Fig. 18 (left panel) presents V_p and V_s 1D average profiles, along with their respective standard deviations that represent wave speed variability (independently from uncertainty) as a function of depth. The relative standard deviation calculated in percent of the mean at a given depth (Fig. 18, middle panel) appears to be as high as $\sim 20\%$ in the upper crust, decreases down to $\sim 5\%$ at the upper to lower crust transition, and is $\sim 10\%$ in the lower crust. Mantle wave speed anomalies, on the other hand, are characterized by lower values (i.e. they show less lateral variability) than those of the crust, with a standard deviation of $\sim 1-2\%$ only, thus evidencing the expected higher petrological homogeneity of the mantle with respect to the crust. Finally, the right panel of Fig. 18 shows the evolution of the average wave speed standard deviation with depth. It differs from the middle panel in that it does not show lateral variability but instead provides an estimate of the average uncertainty at that depth. From that plot it appears that the largest uncertainties are observed at shallow depth, with values as high as 20% at the

	Research and Development Program on Seismic Ground Motion	Ref : SIGMA2-2018-D2-014
		Page 15/27

surface. They decrease gradually from the surface down to a value of ~4% at 10 km, and reach a value of ~1-2 %, from 40 km to 100 km, i.e. at mantle depths, for both Vp and Vs.

This dependence of uncertainty with depth is also visible from the maps shown in Fig. 11 and 13. The largest standard deviation values are found at shallow depth, and more particularly above 10 km. It is also in that part of the model that the uncertainty field is affected by the largest variability: on the 0 and 5 km slices, the contrast between crystalline basement and sedimentary basins is quite clear, especially at 5 km where the offshore basins exhibit the highest uncertainties, thus evidencing the lack of agreement between input models in those regions, where substantial improvements could be achieved in the future.

The characteristics of our model (including uncertainties) reflect those of the input grids we averaged and the choices and assumptions that we made at different stages: the choice of the Moho modeling procedure, the decision to model crust and mantle separately, the input models we selected, the Vp/Vs ratio model we considered, and most importantly the weighting scheme that we adopted. Different choices could have been made, which would have led to a different final output. A sensitivity analysis could for instance have been performed to establish the model variability that could have resulted from all reasonable other choices. We emphasize that this one model combines tomographic results that hold information from various seismological data types and data sets, and is therefore, *de facto*, an improvement over 1D models for earthquake location. The extent of this improvement, however, both in terms of accuracy and precision, still needs to be assessed.

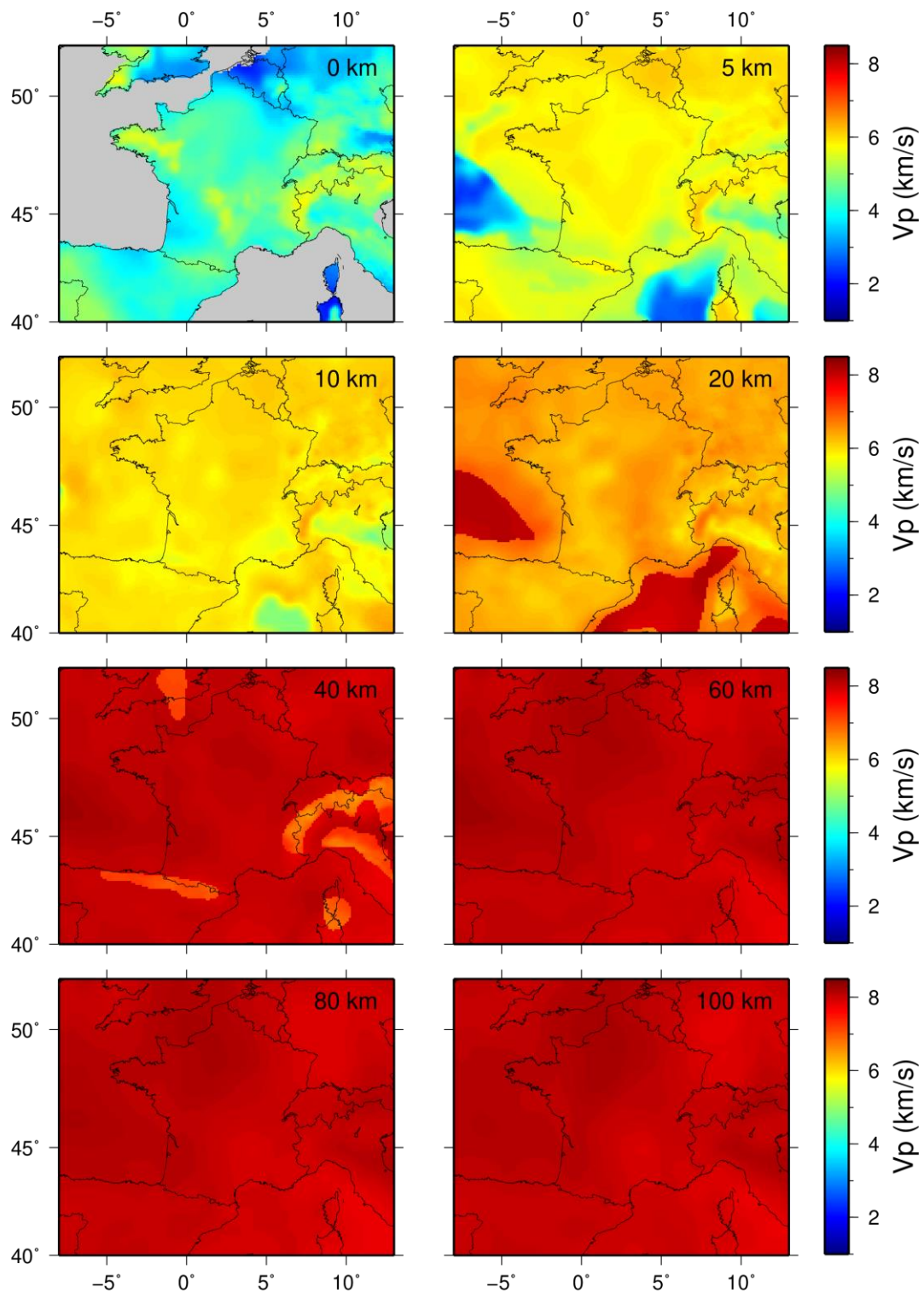


Figure 10. Depth slices through the P-wave component of our model. See text for details. Note that the 10 km x 10 km grid has been resampled to 1 km x 1 km for display purpose. See Fig. 3 for a comparison with EPcrust reference model.

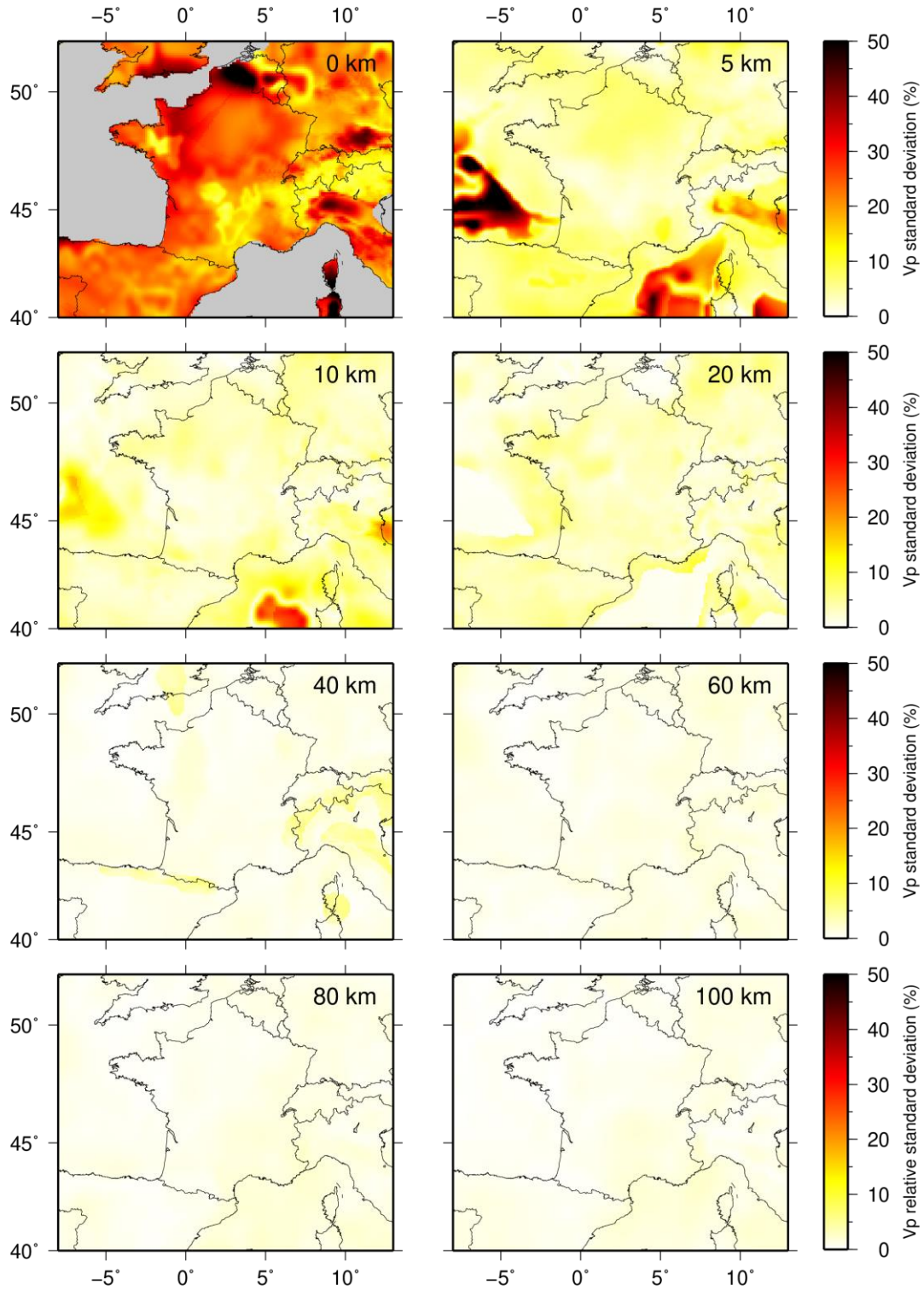


Fig. 11. Maps of Vp weighted standard deviation expressed in percent of the mean Vp values shown in Fig. 10.

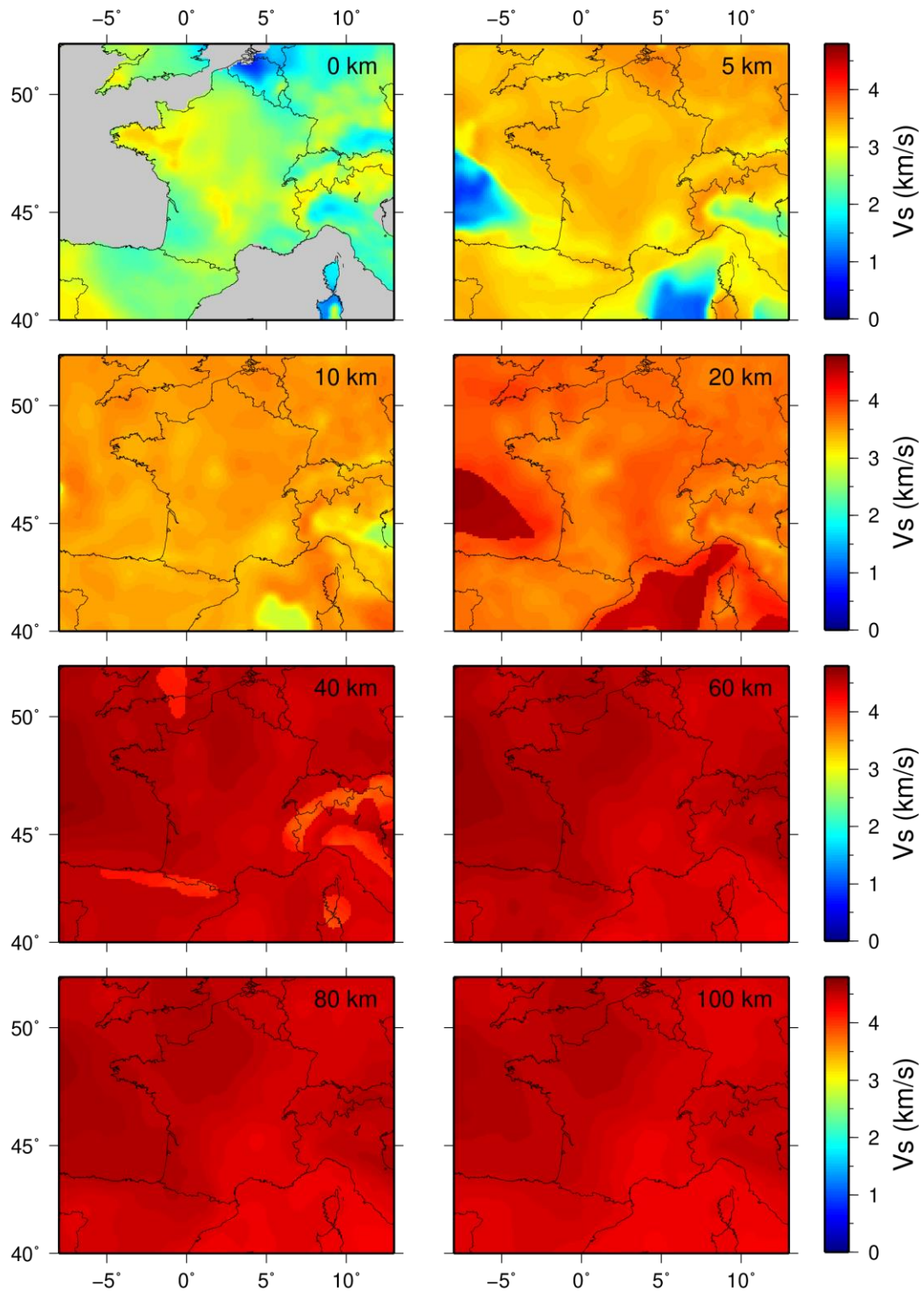


Figure 12. Depth slices through the S-wave component of our model. See text for details. . Note the 10 km x 10 km grid has been resampled to 1 km x 1 km for display purpose. See Fig. 4 for a comparison with EPcrust reference model.

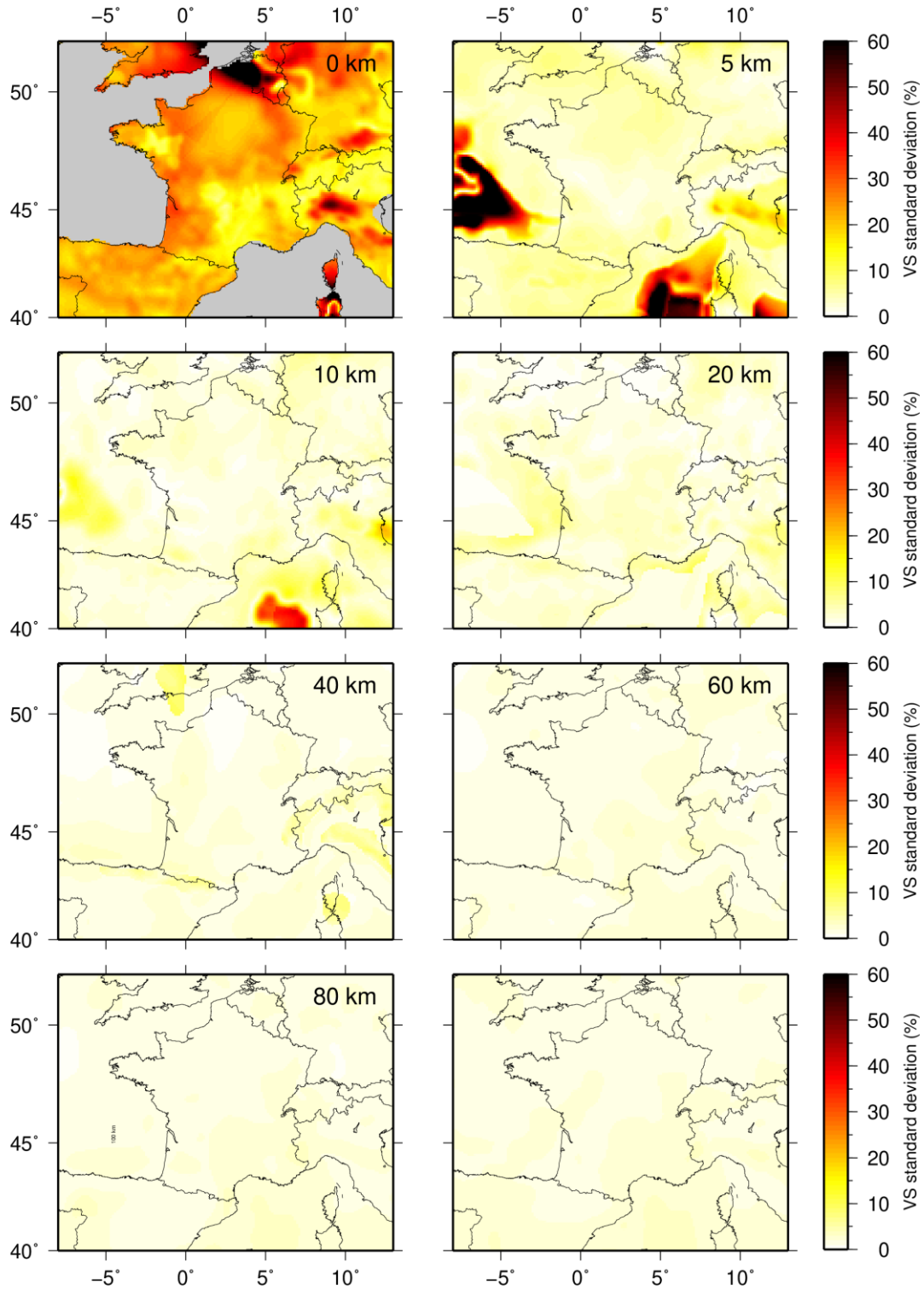


Fig. 13. Maps of Vs weighted standard deviation expressed in percent of the mean Vs values shown in Fig. 12.

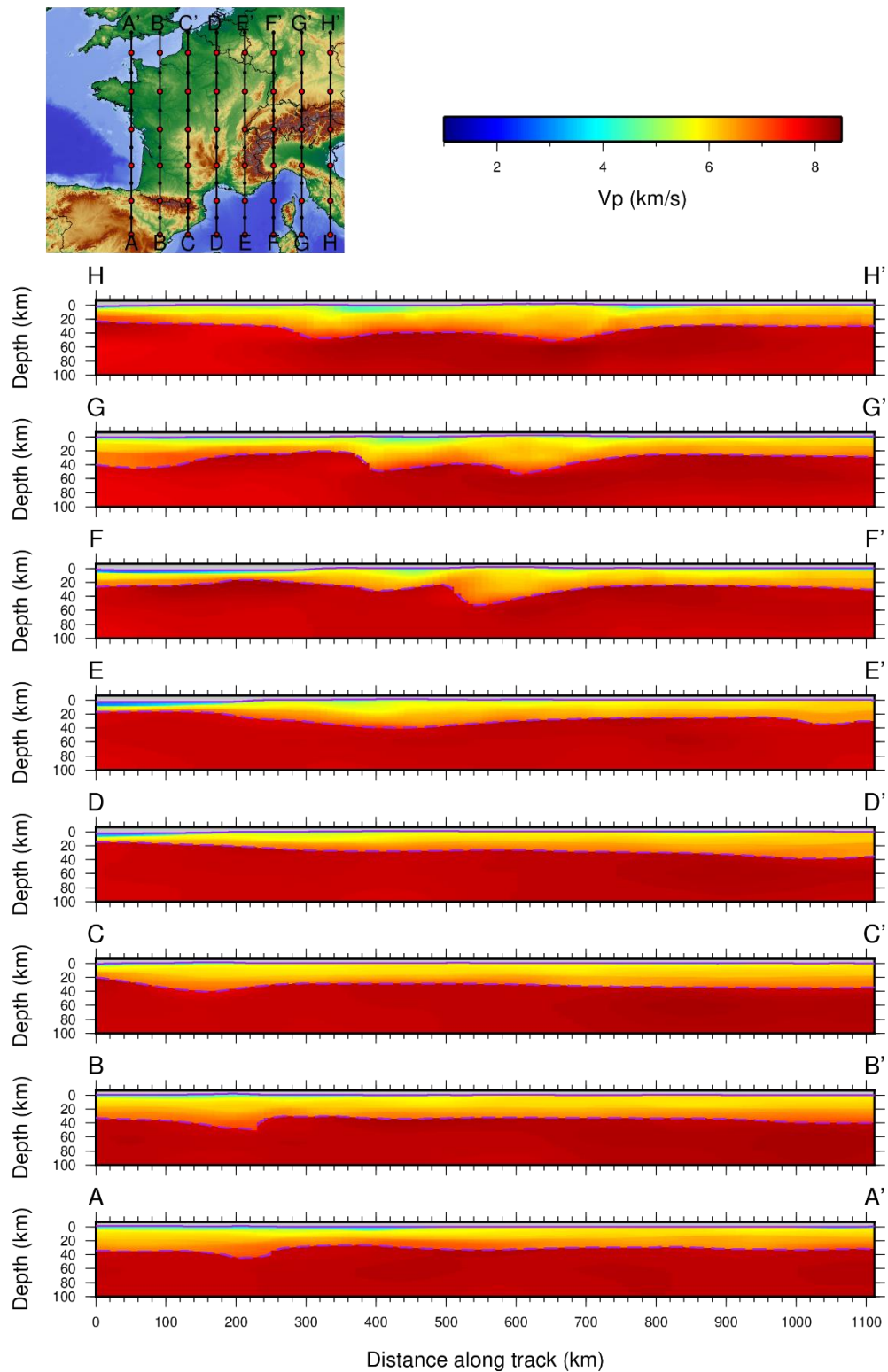


Figure 14. North-South cross-section through the P-wave component of our model. See text for details.

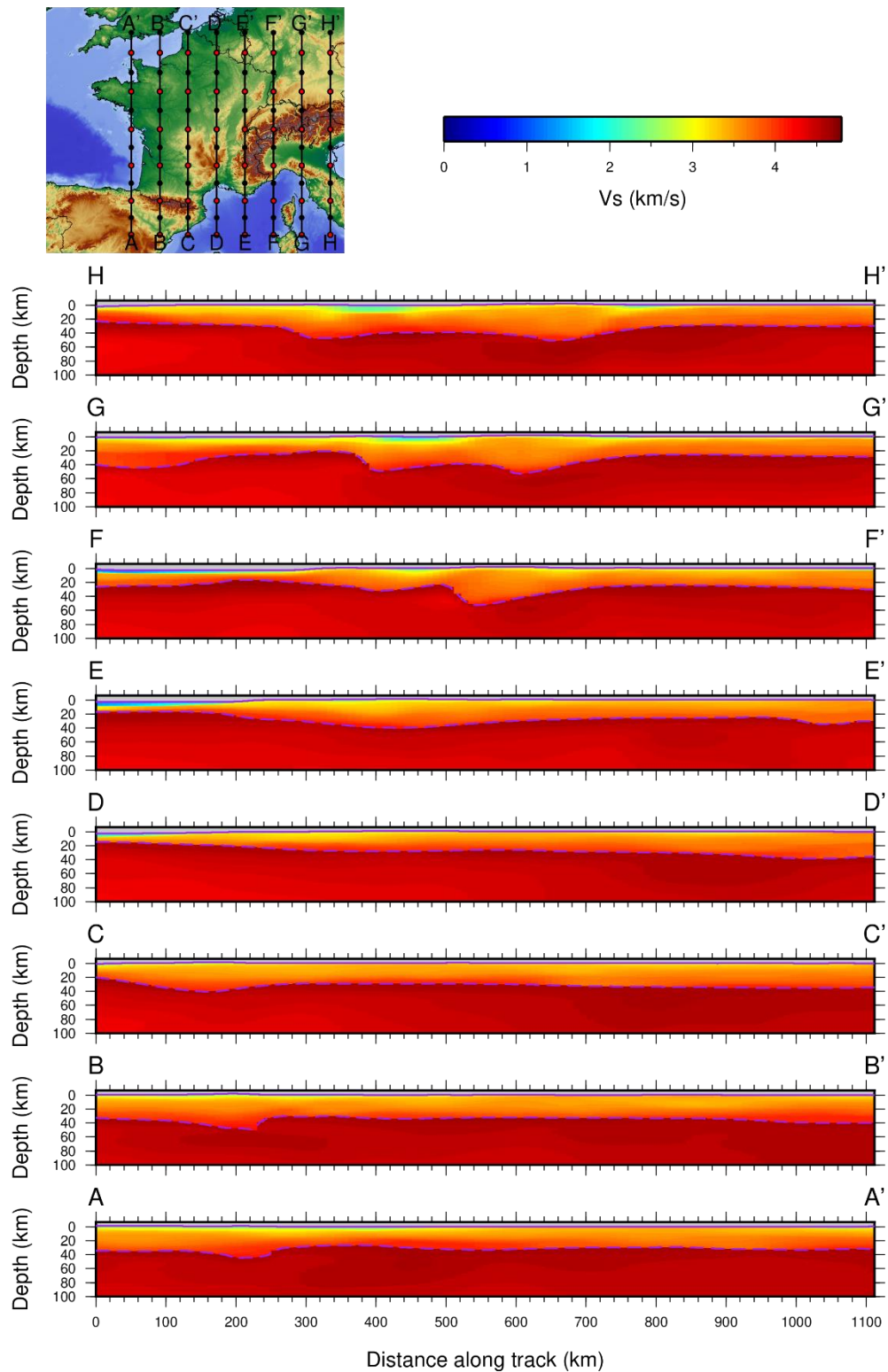


Figure 15. North-South cross-sections through the S-wave component of or model. See text for details.

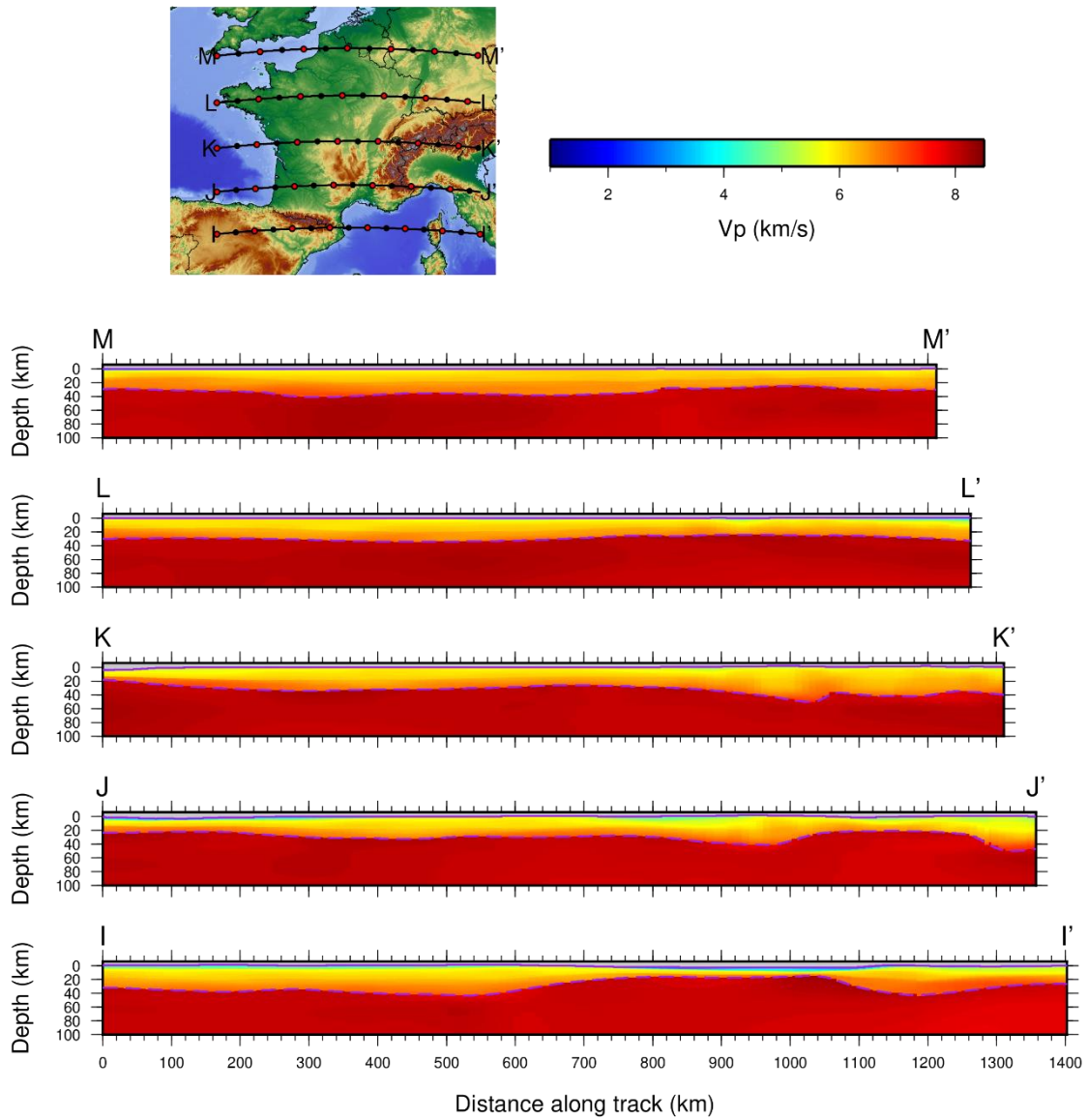


Figure 16. East-West cross-sections through the P-wave component of our model. See text for details.

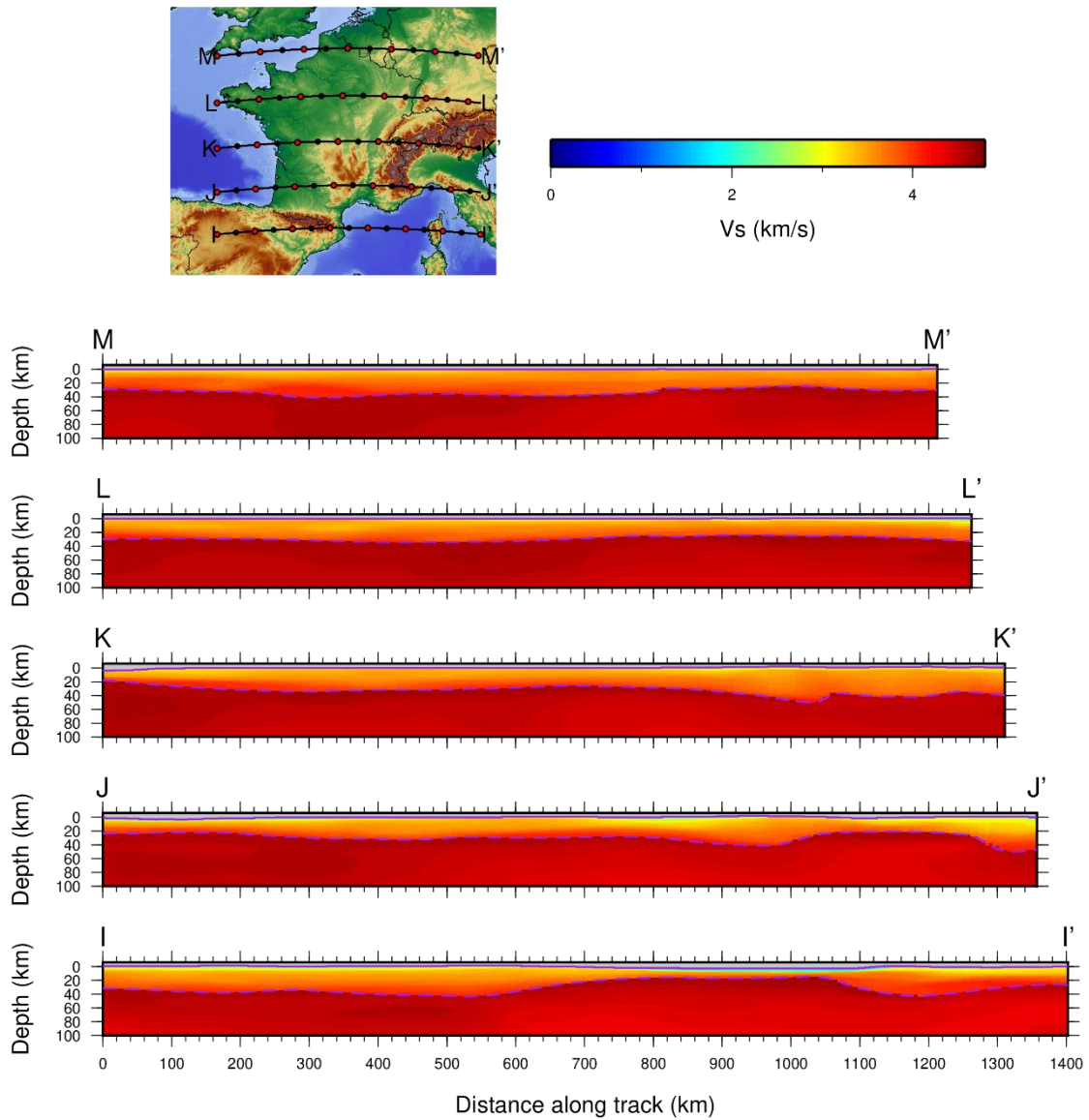


Figure 17. East-West cross-section through the S-wave component of our model. See text for details.

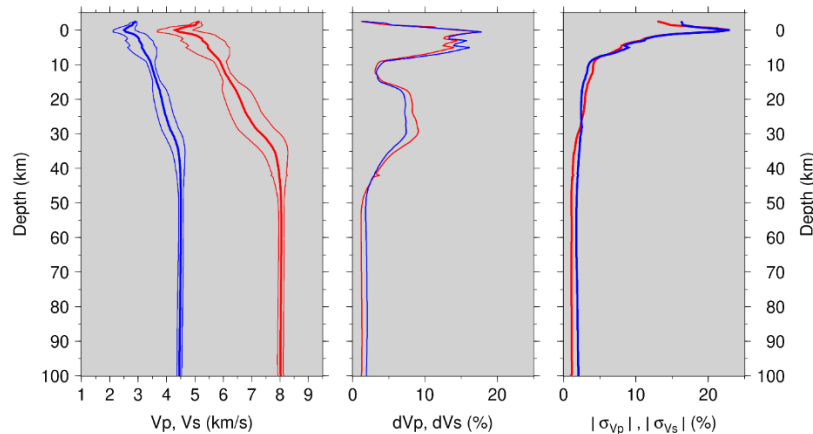


Figure 18. Left : 1D Average P- (red) and S- (blue) wave speed depth profiles (thick line), along with their corresponding standard deviations (thinner lines). Middle : Relative standard deviation of the 1D Vp and Vs profiles shown on the left panel, expressed in percentage of the mean P- and S-wave speed. Right: Mean relative standard deviation of P- and S-wave speed as a function of depth.

5. Conclusion and future work

We built a preliminary 3D P- and S-wave seismological model for Metropolitan France and neighbouring regions, primarily aimed at earthquake location. The model includes two explicit interfaces, the topography/bathymetry and Mohorovičić discontinuity, respectively. P- and S-wave speeds were calculated as a weighted average of previously published tomographic models, and the crust and mantle were modeled separately so realistic gradients could be modeled across the Moho. In addition, weighted standard deviation was computed at each node of the grid and provides an estimate of wave speed uncertainty values, along with their spatial variations. The model can be used with 3D earthquake location procedures that consider interfaces (e.g. Wagner et al., 2013) or not (e.g. Lomax et al., 2000). It can also be used to extract mean or median 1D models to be used with more classical 1D techniques (e.g. Lienert et al., 1983).

Whether this model will actually improve earthquake location quality still needs to be assessed. We will investigate this question in future work, using arrival time data from quarry blasts identified on the French Metropolitan territory (Cara et al., 2015) and for which the quarry at the origin of the explosion is known. Relocation of catalogue earthquakes in regions where local, dense arrays have been temporarily deployed to record aftershock sequences (e.g. Perrot et al., 2005), will also be carried out to help assess potential improvements that could arise from the use of our model. More simply, travel time residual and hypocentral solution covariance matrix analysis (with this model and others) should also provide some information about this question, and so should a comparison of relocated hypocenter spatial distribution with known tectonic features.

This model is aimed at evolving. For instance, two recent local earthquake tomographic studies, one in the Pyrenees and the other one in the Alps, have not been included because they have not been published yet: as soon as they have, they will be included in our model. The ongoing development of a permanent broadband seismic network evenly covering the French Metropolitan territory (in the framework of RESIF, the French seismological and geodetic network) should also eventually lead to additional information about crustal structure that will make this model evolve. Ideally, we would also like to include information from seismic profiles and borehole databases: it should help constrain the shallow part of the model, where the largest uncertainties are observed. Finally, we are also planning to update the model after relocation by means of local earthquake tomography.

6. References

- Amante, C., and B. Eakins, 2009. Etopo1 1 arc-minute global relief model: Procedures, data sources and analysis, Tech. rep., NOAA Technical Memorandum NESDIS NGDC-24. National Geophysical Data Center, NOAA.
- Bodin, T., Salmon, M., B. L. N. Kennett and M. Sambridge, 2012. Probabilistic surface reconstruction from multiple data sets: An example for the Australian Moho, *J. Geophys. Res.*, 117, B10307.
- Cara, M., Cansi, Y., Schlupp, A., Arroucau, P., Béthoux, N., Beucler, E., Bruno, S., Calvet, M., Chevrot, S., Deboissy, A., Delouis, B., Denieul, M., Deschamps, A., Doubre, C., Fréchet, J., Godey, S., Golle, O., Grunberg, M., Guilbert, J., Haugmard, M., Jenatton, L., Lambotte, S., Leobal, D., Maron, C., Mendel, V., Merrer, S., Macquet, M., Mignan, A., Mocquet, A., Nicolas, M., Perrot, J., Potin, B., Sanchez, O., Santoire, J.-P., Sèbe, O., Sylvander, M., Thouvenot, F., Van der Woerd, and K. Van der Woerd, 2015. SI-Hex: a new catalogue of instrumental seismicity for metropolitan France, *Bull. Soc. Géol. France*, 186(1), 3-19.
- Chamot-Rooke, N., Jestin, F., and J.-M. Gaulier, 1997. Constraints on Moho depth and crustal thickness in the Liguro-Provençal Basin from a 3D gravity inversion: geodynamic implications, *Revue de l'Institut Français du Pétrole*, 52(6), 557-583.
- Chevrot, S., Villaseñor, A., Sylvander, M., Benahmed, S., Beucler, E., Cougoulat, G., Delmas, P., de Saint Blanquat, M., Diaz, J., Gallart, J., Grimaud, F., Lagabrielle, Y., Manatschal, G., Mocquet, A., Pauchet, H., Paul, A., Péquegnat, C., Quillard, O., Roussel, S., Ruiz, M., and D. Wolyniec, 2014. High-resolution imaging of the Pyrenees and Massif Central from the data of the PYROPE and IBERARRAY portable array deployments, *J. Geophys. Res. (Solid Earth)*, 119, 6399-6420.
- Diaz, J., and J. Gallart, 2009. Crustal structure beneath the Iberian Peninsula and surrounding waters: A new compilation of deep seismic sounding results, *Phys. Earth and Planet. Int.*, 173(1-2), 181-190.
- Diaz, J., Gil, A. and J. Gallart, 2013. Uppermost mantle seismic velocity and anisotropy in the Euro-Mediterranean region from Pn and Sn tomography, *Geophys. J. Int.*, 192(1), 248-259.
- Diehl, T., Husen, S., Kissling, E., and N. Deichmann, 2009. High-resolution 3-D P-wave model of the Alpine crust, *Geophys. J. Int.*, 179, 1133-1147.
- Gaudot, I., 2016. Analyse des intercorrélations du champ d'onde sismique ambient – Application à la tomographie de l'Ouest de la France, PhD Thesis, University of Nantes.
- Geissler, W. H., Kind, R., and X. Yuan, 2008. Upper mantle and lithospheric heterogeneities in central and eastern Europe as observed by teleseismic receiver functions, *Geophys. J. Int.*, 174, 351-376.
- Giardini, D., Woessner, J., and L. Danciu, 2014. Mapping Europe's Seismic Hazard, *EOS*, 95(29), 261-262.
- Green, P., 1995. Reversible jump MCMC computation and Bayesian model selection, *Biometrika*, 82, 711-732.
- Green, P., 2003. Trans-dimensional Markov chain Monte Carlo, *Highly Struct. Stochastic Syst.*, 27, 179-198.
- Kästle, E. D., El-Sharkawy, A., Boschi, L., Meier, T., Rosenberg, N., Bellahsen, N., Cristiano, L., and C. Weidle, 2018. Surface-wave tomography of the Alps using Ambient-Noise and Earthquake Phase-Velocity Measurements, *J. Geophys. Res.*, 123, 1770-1792.
- Kennett, B. L. N., Engdahl, E. R., and R. Buland, 1995. Constraints on seismic velocities in the Earth from travel times, *Geophys. J. Int.*, 122, 108-124.

Knapmeyer-Endrun, B., Krüger, F., and the PASSEQ Working Group, 2014. Moho depth across the Trans-European Suture Zone from P- and S-receiver functions, *Geophys. J. Int.*, 197, 1048-1075.

Licciardi, 2016. Multi-scale imaging of the crust with teleseismic receiver functions: seismic structure and anisotropy, PhD Thesis, University College Dublin.

Lienert, B. R., Berg, E., and L. N. Frazer, 1986. Hypocenter: An earthquake location method using centered, scaled, and adaptively damped least squares, *Bull. Seism. Soc. Am.*, 76(3), 771-783.

Lombardi, D., Braunmiller, J., Kissling, E., and D. Giardini, 2008. Moho depth and Poisson's ratio in the Western-Central Alps from receiver functions, *Geophys. J. Int.*, 73(1), 249-264.

Lomax, A., Virieux, J., Volant, P., and C. Berge-Thierry, 2000. Probabilistic earthquake location in 3D and layered models : Introduction of a Metropolis-Gibbs method and comparison with linear locations, in *Advances in Seismic Event Location*, Thurber, C.H., and N. Rabinowitz (eds.), Kluwer, Amsterdam, 101-134.

Lu, Y., Stehly, L., Paul, A., and AlpArray Working Group, 2018. High-resolution surface wave tomography of the European crust and uppermost mantle from ambient seismic noise, *Geophys. J. Int.*, 214, 1136-1150.

Manchuel, K., Traversa, P., Baumont, D., Cara, M., Nayman, E., and C. Durouchoux, 2018. The French seismic CATalogue (FCAT-17), *Bull. Earthquake Eng.*, 16, 2227-2251.

Mancilla, F. de L., and J. Díaz, 2015. High resolution Moho topography map beneath Iberia and northern Morocco from receiver functions analysis, *Tectonophysics*, 663, 205-213.

Mele, G., Di Luzio, E., and C. Di Salvo, 2013, Mapping Moho depth variations in Central Italy from PS_{Moho}-P delay times: Evidence of an E-W transition in the Adriatic Moho at 42°N latitude, *Geochem. Geophys. Geosyst.*, 14, 3929-3938.

Macquet, M., Paul, A., Pedersen, H. A., Villaseñor, A., Chevrot, S., Sylvander, M., Wolyniec, D., and PYROPE working group, 2014. Ambient noise tomography of the Pyrenees and the surrounding regions: inversion for a 3-D Vs model in the presence of a very heterogeneous crust, *Geophys. J. Int.*, 199-402-415.

Molinari, I. and A. Morelli, 2011. EPcrust: a reference crustal model for the European Plate, *Geophys. J. Int.*, 185, 352-364.

Monna, S., Cimini, G. B., Montuori, C., Matias, L., Geissler, W. H., and P. Favali, 2013. New insights from seismic tomography on the complex geodynamic evolution of two adjacent domains: Gulf of Cadiz and Alboran Sea, *J. Geophys. Res. (Solid Earth)*, 118, 1587-1601.

Palomeras, I., Villaseñor, A., Thurner, S., Levander, A., Gallart, J., and M. Harnafi, 2017. Lithospheric structure of Iberia and Morocco using finite-frequency Rayleigh wave tomography from earthquakes and seismic ambient noise, *Geochem. Geophys. Geosyst.*, 18, 1824-1840.

Pasyanos, M. E., Masters, T. G., Laske, G., and Z. Ma, 2014. An updated crust and lithospheric model of the earth, *J. Geophys. Res. (Solid Earth)*, 119(3), 2153-2173.

Perrot, J., Arroucau, P., Guilbert, J., Déverchère, J., Mazabraud, Y., Rolet, J., Mocquet, A., Mousseau, M., Matias, L., 2005. Analysis of the Mw 4.3 Lorient earthquake sequence : a multidisciplinary approach to the geodynamics of the Armorican Massif, westernmost France, *Geophys. J. Int.*, 162(3), 935-950.

Potin, B., 2016. Les Alpes Occidentales: tomographie, localization de séismes et topographie du Moho, PhD Thesis, Université Grenoble Alpes.

Rawlinson, N., Reading, A. M., and B. L. N., Kennett, 2006. Lithospheric structure of Tasmania from a novel form of teleseismic tomography, *J. Geophys. Res.*, 111, B02301.

Schivardi, R. and A. Morelli, 2011. EPmantle: a 3-D transversely isotropic model of the upper mantle under the European plate, *Geophys. J. Int.*, 185, 469-484.

Shapiro, N. M., Campillo, M., Stehly, L., Ritzwoller, M. H., 2005. High-Resolution Surface-Wave Tomography from Ambient Seismic Noise, *Science*, 307(5715), 1615-1618.

Sichien, E., Henriot, J.-P., Camelbeeck, T., and B. DE Baets, 2012. Estimating crustal thickness in Belgium and surrounding regions from Moho-reflected waves, *Tectonophysics*, 105-119.

Spada, M., Bianchi, I., Kissling, E., Piana Agostinetti, N., Wiemer, S., 2013. Combining controlled-source seismology and receiver function information to derive 3-D Moho topography for Italy, *Geophys. J. Int.*, 194, 1050-1068.

Stipčević, J., Tkalčić, H., Herak, M., Markušić, S. and D. Herak, 2011. Crustal and uppermost mantle structure beneath the External Dinarides, Croatia, determined from teleseismic receiver functions, *Geophys. J. Int.*, 185, 1103-1119.

Theunissen, T., Chevrot, S., Sylvander, M., Monteiller, V., Calvet, M., Villaseñor, A., Benahmed, S., Pauchet, H., and F. Grimaud, 2018. Absolute earthquake locations using 3-D versus 1-D velocity models below a local seismic network : example from the Pyrenees, *Geophys. J. Int.*, 212, 1806-1828.

Wagner, M., Husen, S., Lomax, A., Kissling, E., and D. Giardini, 2013. High-precision earthquake locations in Switzerland using regional secondary arrivals in a 3-D velocity model, 193, 1589-1607.

Yudistira, T., 2015. The crustal structure beneath the Netherlands inferred from ambient seismic noise, PhD Thesis, University of Utrecht.